Engineering 30 (2023) 190–202

Contents lists available at ScienceDirect

Engineering

journal homepage: www.elsevier.com/locate/eng

Research
Medical Engineering—Article

Therapeutic Characterization of ^{131}I-Labeled Humanized Anti-B7-H3 Antibodies for Radioimmunotherapy for Glioblastoma

Fengqing Fu [a,b,#], Meng Zheng [c,e,#], Shandong Zhao [c,e,#], Yan Wang [b,c,e], Minzhou Huang [c,e], Hanqing Chen [f], Ziyi Huang [a,b], Kaijie Zhang [c,e], Liyan Miao [c,e,*], Xueguang Zhang [a,b,d,*]

[a] Jiangsu Institute of Clinical Immunology, the First Affiliated Hospital of Soochow University, Suzhou 215000, China
[b] State Key Laboratory of Radiation Medicine and Protection, Soochow University, Suzhou 215123, China
[c] Department of Clinical Pharmacology, The First Affiliated Hospital of Soochow University, Suzhou 215006, China
[d] Suzhou Bright Scistar Antibody Biotech. Co., LTD., Suzhou 215152, China
[e] Institute for Interdisciplinary Drug Research and Translational Sciences, College of Pharmaceutical Sciences, Soochow University, Suzhou 215123, China
[f] Department of Hematology, the First Affiliated Hospital of Soochow University, Suzhou 215000, China

ARTICLE INFO

Article history:
Received 11 January 2023
Revised 4 April 2023
Accepted 16 May 2023
Available online 12 June 2023

Keywords:
B7-H3
Radioimmunotherapy
Glioblastoma
Pharmacokinetics
Pharmacodynamics

ABSTRACT

B7 homolog 3 (B7-H3) has attracted much attention in glioblastoma (GBM) radioimmunotherapy (RIT) due to its abnormally high expression on tumor cells. In this study, we report that two specific humanized anti-human B7-H3 antibodies (hu4G4 and hu4H12) derived from mouse anti-human B7-H3 antibodies that were generated by computer-aided design and exclusively recognize membrane expression of B7-H3 by human glioma cells. Hu4G4 and hu4H12 were radiolabeled with ^{89}Zr for RIT antibody screening. Micro-positron emission tomography (PET) imaging, biodistribution and pharmacokinetic (PK) analyses of ^{89}Zr-labeled antibodies were performed in U87-xenografted models. ^{125}I labelling of the antibodies for single-photon emission computed tomography (SPECT) imaging was also used to investigate the biological behavior of the antibodies *in vivo*. Furthermore, the pharmacodynamic (PD) of the ^{131}I-labeled antibodies were evaluated in U87-xenografted mice and GL261 Red-FLuc-B7-H3 *in situ* glioma tumor models. Micro-PET imaging and biodistribution analysis with a gamma counter showed that ^{89}Zr-deferoxamine (DFO)-hu4G4 had higher tumor targeting performance with lower liver uptake than ^{89}Zr-DFO-(hu4H12, immunoglobulin G (IgG)). The biodistribution results of ^{125}I-SPECT imaging were similar to those of ^{89}Zr-PET imaging, though the biodistribution in long bone joints and the thyroid varied. The PD analysis results indicated that ^{131}I-hu4G4 had an excellent therapeutic effect and high safety with no apparent toxicity. Interestingly, ^{131}I-hu4G4 improved the tumor vasculature in tissues with higher expression of collagen type IV and platelet-derived growth factor receptor β (PDGFR-β) compared with control treatment, as determined by immunofluorescence (IF), which contributed to inhibiting tumor growth. Taken together, our data indicate that hu4G4 exhibits good tumor targeting and specificity, achieves low nonspecific concentrations in normal tissues, and has acceptable PK characteristics. ^{131}I-hu4G4 also exerts effective antitumor effects with an ideal safety profile. Therefore, we expect hu4G4 to be an excellent antibody for the development of GBM RIT.

1. Introduction

Glioblastoma (GBM), the most common grade IV glioma, is the most aggressive lethal malignant brain tumor in adults [1,2]. The current standard of care for GBM is Stupp's protocol, comprising surgery, chemotherapy (temozolomide), and external beam radiation therapy (EBRT) [3]. However, the efficacy is limited, and most patients invariably experience recurrence with a median overall survival (OS) time of approximately 15 months [4]. Given these challenges, novel targeted and immune therapies for GBM, such as radioimmunotherapy (RIT), have been met with hope and enthusiasm [5].

RIT, an emerging approach in the field of precision medicine, is a method of targeting therapeutic molecules with radioconjugated antibodies to kill tumor cells [6]. RIT has advantages

* Corresponding authors.
E-mail addresses: miaolysuzhou@163.com (L. Miao), xueguangzh@126.com (X. Zhang).
# These authors contributed equally to this work.

https://doi.org/10.1016/j.eng.2023.05.011

for the treatment of local, metastatic, or diffuse tumors and permits the delivery of a high dose of therapeutic radiation to cancer cells while minimizing the exposure of normal cells compared to conventional EBRT [7]. Two monoclonal antibodies (mAbs), [^{90}Y] ibritumomab tiuxetan (Zevalin®) and [^{131}I] itositumomab (Bexxar®), were approved by the Food and Drug Administration (FDA) in 2002 and 2003, respectively, for the RIT of relapsed and refractory non-Hodgkin lymphoma [8]. To date, several preclinical studies have shown that RIT has a promising therapeutic effect in the treatment of solid tumors, such as breast cancer [9], pancreatic cancer [10], and small-cell lung cancer [11]. Therefore, RIT is a novel option for GBM treatment. However, the selection and design of antibodies for targeting are critical to the therapeutic effect of RIT, and factors such as the specific properties, affinity, tumor-to-blood ratio, and immunogenicity of the antibody need to be considered [12].

B7 homolog 3 (B7-H3), a transmembrane protein encoded by the cluster of differentiation 276 (*CD276*) gene, is a checkpoint molecule from the B7 family. B7-H3 is highly expressed in human malignancies and tumor vasculature but demonstrates low expression in normal tissues, which makes it an appealing target and prognostic tumor marker [13–15]. In Chinese Glioma Genome Atlas (CGGA) and Gene Expression Profiling Interactive Analysis (GEPIA) data [16], B7-H3 is upregulated more in higher-grade gliomas than in lower-grade gliomas [17], which is consistent with our previous studies showing that B7-H3 was overexpressed in 94.7% of 57 glioma patients with poor clinical outcomes.

At present, the antibodies targeting B7-H3 being developed for use in targeted RIT mainly include the mAbs 4H7, 376.96, and 8H9, which have exhibited high tolerability and encouraging therapeutic effects in the treatment of a variety of solid tumors; furthermore, some are currently being tested in clinical trials. Specifically, the 8H9 mAb (omburtamab), as a humanized murine mAb, has been granted breakthrough therapy designation by the FDA [18]. The convection-enhanced delivery of ^{124}I-8H9 into children with diffuse intrinsic pontine glioma was proven to be safe (NCT01502917), and ^{131}I-omburtamab achieved excellent responses for patients with central nervous system (CNS) metastases of neuroblastoma [19]. These results indicate that B7-H3 is a safe and feasible target for RIT in GBM.

We generated a total of 53 mouse anti-human B7-H3 antibodies. Upon screening, we selected two mouse anti-human B7-H3 antibodies (4G4 and 4H12) that exclusively recognized membrane expression of B7-H3 by human glioma cells to construct humanized anti-B7-H3 antibodies (hu4G4 and hu4H12). Then, we established an antibody screening strategy based on positron emission tomography (PET) imaging profiles of ^{89}Zr-hu4G4 and ^{89}Zr-hu4H12 to assess the biological behavior of the antibodies in rodent tumor models. As the *in vivo* biodistribution of the ^{131}I labeled antibody was consistent with that of the ^{125}I-labeled antibody, we investigated the dynamic biodistribution of hu4G4 and hu4H12 by noninvasive ^{125}I-single-photon emission computed tomography (SPECT) imaging.

More importantly, to lay a foundation for later clinical translation, pharmacodynamic (PD) and safety profile studies of the humanized anti-B7-H3 mAbs labeled with the therapeutic radionuclide ^{131}I were carried out when the mAbs were used for RIT in GBM tumor-bearing mice. Our results indicate that hu4G4 is a promising therapeutic antibody with excellent tumor targeting capacity and specificity achieving low nonspecific concentrations in normal tissues and with acceptable pharmacokinetic (PK) properties. ^{131}I-hu4G4 exerts potent antitumor activity with a good safety profile.

2. Materials and methods

The detailed descriptions of each reagent, cell culture, experimental animal, tumor models, and material are provided in Sections S1.1–S1.3 in Appendix A. All procedures involving mice and experimental protocols were approved by Soochow University Institutional Animal Care.

2.1. Antibody humanization

To decrease the immunogenicity of the murine antibodies hu4G4 and hu4H12 derived from hybridoma technology, humanization was carried out using Discovery Studio (Dassault systems, France). Three dimensional (3D) structures of the murine and humanized antibodies, including the variable domain of the heavy chain (VH) and light chain (VL), were constructed. Fv fragments were modeled using computer-guided homology modeling. The 3D structures of hu4G4/hu4H12 and the humanized antibodies were compared to those of huhu4G4/huhu4H12 using the structural superimposition method.

2.2. Antibody expression and purification

The sequences of the VH and VL were subcloned into the full-length immunoglobulin G1 (IgG1) expression vector to generate plasmids encoding VH and VL of hu4G4 and hu4H12, which were transfected into ExpiCHO-S cells. At 18 h after transfection, ExpiFectamine CHO Enhancer (Life Technologies, USA) was added. After 7 d, the supernatant was harvested. Hu4G4 and hu4H12 were purified by protein A affinity chromatography. The concentration of the purified antibodies was determined using a BioDrop spectrophotometer (Biochrom Ltd., UK) and a BCA protein assay kit (Beyotime, China).

2.3. Antibody affinity determination

Different series of human B7-H3 concentrations (100.0000–1.5625 nmol·L^{-1}) were prepared by two-fold serial dilution. A Biacore 8K surface plasmon resonance (SPR) system (GE Healthcare Bio-Sciences, USA) equipped with different sensor chip types and flat (Biacore C1 and Xantec CMD-P) and 3D-hydrogels (Biacore CM5 and Xantec CMD-200M), was used to determine the binding kinetic rate and affinity constants at 25 °C and in a running buffer of HBS-EP$^+$ (10 mmol·L^{-1} 4-(2-hydroxyethyl)-1-piperazineethanesulfonic acid (HEPES), pH 7.4, 150 mmol·L^{-1} NaCl, 3 mmol·L^{-1} ethylenediaminetetraacetic acid (EDTA), 0.05% Tween-20). The data were processed and analyzed with Biacore 8K Evaluation Software Version 1.0 (GE Healthcare Bio-Sciences, USA).

2.4. ^{89}Zr radiolabeling of deferoxamine (DFO)-B7-H3 antibodies

For ^{89}Zr radiolabeling, B7-H3-targeted antibodies (hu4G4 and hu4H12) and IgG mAb were conjugated to p-SCN-DFO (Macrocyclics, USA) using traditional methods with some modifications [20]. Briefly, a fifteen-fold molar excess of DFO (in 20–30 μL dimethyl sulfoxide) was added to the antibody and stirred slowly at 37 °C. After 90 min of reaction, DFO-conjugated antibodies (DFO-hu4G4, DFO-hu4H12, and DFO-IgG) were purified using a PD-10 column (Cytiva, USA).

DFO-conjugated antibodies were radiolabeled with ^{89}Zr using a method previously reported with some modifications [20]. Briefly, 10–20 μL of ^{89}Zr-oxalate stock solution (11–17 megabecquerel (MBq)) was diluted with a nine fold volume of 0.1 mol·L^{-1} HEPES, the pH was adjusted to 7.0 with 0.1 mol·L^{-1} Na_2CO_3 solution, and DFO-conjugated antibody was then added and incubated for 0.5 h at 37 °C. PD-10 columns were used for purification with 0.15 mol·L^{-1} acetate buffer (pH 7.2), and the radiochemical purity (RCP) of ^{89}Zr-labeled DFO-B7-H3 antibodies was measured by radio-instant thin-layer chromatography (radio-TLC; Bioscan Inc.,

USA) using 0.5 mol·L^{-1} citrate buffer at pH 5.0 as the mobile phase and glass fiber paper as the carrier.

2.5. PET imaging with ^{89}Zr-labeled DFO-B7-H3 antibodies

The whole-body distribution of the antibody in tumor-bearing mice was examined with an Inveon micro-PET scanner (Siemens, Germany). U87-xenografted mice randomized into five groups of six mice were intravenously injected with ^{89}Zr-DFO-B7-H3 (hu4G4 and hu4H12) ((1.68 ± 0.11) MBq, 1.75 mg·kg^{-1} bodyweight), ^{89}Zr-DFO-IgG ((1.43 ± 0.08) MBq, 1.75 mg·kg^{-1} bodyweight), ^{89}Zr-DFO ((1.05 ± 0.21) MBq), or ^{89}Zr-oxalate ((2.16 ± 0.11) MBq) and placed on the scanner bed under 1%–2% isoflurane anesthesia. Then, 10 min static PET images were acquired at 2, 12, 24, 48, 72, 96, 120, 144, and 168 h postinjection. The images were reconstructed using the ordered subset expectation maximization 3D (OSEM3D) algorithm. The percentage injected dose per gram of tissue (%ID/g) in regions of interest (ROIs) drawn over the tumors main organs and was measured using an Inveon Research Workplace ASIPro (Siemens Medical Solution, Germany) workstation.

2.6. Biodistribution and PK characteristics of ^{89}Zr-labeled antibodies

For the biodistribution study, tumor-bearing mice were dissected at 72 and 168 h postinjection after PET imaging, and the major organs and tissues of each mouse, such as blood, brain, heart, liver, spleen, kidney, bone, long bone joints, muscle, stomach, intestine, gonad, and tumor samples, were collected and counted using a gamma counter (n = 3) (2480 WIZARD; PerkinElmer, USA).

For the PK study, blood samples were collected from the tail (10–20 μL per animal) at 5, 10, 15, and 30 min; and 1, 2, 6, 24, 48, 72, 96, 120, 144, and 168 h after injection, weighed immediately and assessed with a gamma counter. PK parameters were analyzed by Phoenix WinNonLin (version 6.4).

2.7. Radiolabeling with ^{131}I and ^{125}I

For ^{131}I radiolabeling, 50 μg of the B7-H3-targeted antibodies hu4G4 and IgG mAb were first dissolved in 100 μL of phosphate buffered saline (PBS, pH 7.4) and mixed with 20 μL of Na^{131}I (approximately 120 MBq). Then, 100 μL of chloramine-T (10 μg·μL^{-1}) was added, the mixture was vortexed for 60 s, and the reaction was then immediately halted using 100 μL of sodium metabisulfite (10 μg·μL^{-1}). The product was purified through a PD-10 column with PBS. The RCP was determined with high-performance liquid chromatography (HPLC) on a Waters e2695 instrument with an online radioactivity detector (FC-3200; Bioscan, USA) using a size exclusion chromatography (SEC) chromatogram (G3000SWXL; TOSOH, Japan). The procedure used for ^{125}I radiolabeling of the antibodies was similar to that used for ^{131}I radiolabeling.

2.8. SPECT imaging and biodistribution analysis with ^{125}I-labeled antibodies

The whole-body distribution of the antibody in tumor-bearing mice was examined by a SPECT scanner (Symbia T16; Siemens) with a pinhole collimator. Twenty U87-xenografted mice were randomized into four groups. Each group of mice was intravenously injected with Na^{125}I ((12.03 ± 0.48) MBq, 1.75 mg·kg^{-1} bodyweight), ^{125}I-hu4G4 ((12.01 ± 0.51) MBq, 1.75 mg·kg^{-1} bodyweight), ^{125}I-IgG ((11.44 ± 0.59) MBq, 1.75 mg·kg^{-1} bodyweight), or ^{125}I-hu4H12 ((11.27 ± 0.24) MBq). After treatment for 2 h, mice were placed on the scanner bed under 1%–2% isoflurane anesthesia. Next, 10 min static SPECT images were acquired at 2, 24, 48, and 72 h postinjection. The images were reconstructed, and the %ID/g values in ROIs of the images were analyzed by PMOD software (version 4.3). Detailed procedures for the *ex vivo* biodistribution assessment of ^{125}I-labelled antibodies are provided in Section S1.5 in Appendix A.

2.9. Dosimetry

As the biodistribution of ^{131}I labeled antibodies is consistent with that of the ^{125}I-labeled antibody *in vivo*, the approximate dosimetry of the tumor after administration of ^{131}I-(hu4G4, hu4H12, IgG) can be calculated based on the SPECT imaging data of ^{125}I-(hu4G4, hu4H12, IgG) [21,22].Therefore, using the tumor uptake (%ID/g) value derived from the SPECT imaging analysis, a conservative estimate of the dose to a tumor following injection of ^{131}I-labeled antibodies was calculated using the dose-to-sphere modeling capabilities of OLINDA/EXM (version 2.1) [23].

2.10. Assessment of the PD characteristics of ^{131}I-labeled antibodies and safety assessments in U87-xenografted mice

2.10.1. Assessment of the antitumor efficacy of ^{131}I-hu4G4 radiotherapy in U87-xenografted mice

U87-xenografted mice with established tumors were randomly divided into four groups (n = 14 per group) and injected with ^{131}I-hu4G4, ^{131}I-IgG, hu4G4, or PBS (negative control) for two cycles every two weeks for a total of three weeks of follow-up, as outlined in Table 1. Four days before administration, these mice were given an oral saturated solution of potassium iodide for thyroid blockade. The tumor volume was measured with a digital caliper during treatment, and the state and survival of the animal models were assessed. Tumor-bearing mice were considered to have died when the tumor volume reached 1000 mm^3.

Furthermore, to evaluate early treatment response, β-2-[^{18}F]-fluoro-2-deoxy-*D*-glucose (^{18}F-FDG) PET imaging was performed before administration (0 d) and at 7 d postinjection after therapy (n = 4 per group). Each group was injected with ^{18}F-FDG, and 5 min static PET images were acquired at 1 h postinjection. The analysis method was similar to that used for PET imaging with an ^{89}Zr-labeled antibody.

2.10.2. Safety assessment of ^{131}I-hu4G4

The body weight of the mice was monitored for systemic radiotherapy-related toxicity. The morphology of the tissues (including the heart, liver, spleen, lung, and kidney) was judged by hematoxylin-eosin (H&E) staining (H&E Staining Kit; Solarbio, China). In addition, blood samples were collected for hematologic analysis via retro-orbital blood draws. White blood cell, red blood cell, and platelet counts were determined using an ADVIA® 2120/2120i (Siemens) and compared with baseline values that were measured prior to administration of the radiotherapy and values reported in Ref. [24].

2.10.3. Immunofluorescence (IF) staining

At the end of treatment, the tumors were collected and used for H&E and IF staining. CD31, platelet-derived growth factor

Table 1
Therapeutic study groups of mice bearing U87 GBM that received a single injection of the given agent.

Study group	Treatment
Control	100 μL of PBS
hu4G4	30 μg of hu4G4 in PBS
^{131}I-hu4G4	11.1 MBq of ^{131}I-hu4G4 with 30 μg of hu4G4
^{131}I-IgG	11.1 MBq of ^{131}I-IgG with 30 μg of IgG

receptor-β (PDGFR-β), and collagen type IV (Col IV) expression were evaluated by IF as described in Section S1.6 in Appendix A.

2.11. Preliminary assessment of the PD characteristics of ^{131}I-labeled antibodies in a mouse GL261 Red-FLuc-B7-H3 in situ glioma tumor model

GL261 Red-FLuc-B7-H3 *in situ* glioma tumor model mice were randomly divided into two groups (n = 8) (Fig. S1 in Appendix A). Each group of mice was intracranially injected with 10 μL of the control (PBS) or 10 μL of ^{131}I-hu4G4 ((1.11 ± 0.02) MBq, 0.15 mg·kg^{-1} bodyweight) after glioma cell implantation. The luciferase expression of the tumor (representing tumor growth) was monitored at different time points using PerkinElmer IVIS® spectroscopy. Mice were imaged 10 min after 15 mg·kg^{-1} fluorescein was injected at different time points and the body weights of the mice were also monitored.

2.12. Statistical analysis

Data analysis was performed using GraphPad Prism (version 9). Quantitative results are presented as the mean ± standard deviation. Student's t test was used for statistical analysis, and p values less than 0.05 were deemed statistically significant.

3. Results

3.1. Expression of B7-H3 on glioma cells recognized by anti-B7-H3 4G4 and 4H12

In our previous study, we found that B7-H3 was significantly expressed in tumor cells, especially in the invading cells of glioma samples, but rarely in normal brain specimens [25]. This finding is consistent with the finding that the anti-B7-H3 antibody 8H9 specifically binds to the majority of tested neuroepithelial tumors [26] and glioma cells [27] but not normal neurons or glia.

We generated a series of mouse anti-human B7-H3 antibodies (53 in total) by following standard immunization protocols. Most of the anti-B7-H3 antibodies recognized the B7-H3 protein on the membrane of glioma cells. Two antibodies, 4G4 and 4H12, showed high reactivity with most glioma cell lines: A172, U87, U251, UW28, and SHG-44 (Fig. S2 in Appendix A). Furthermore, 4G4 and 4H12 were found to specifically bind to U87 wild-type cells but not to *B7-H3* knockout U87 cells. Furthermore, 4G4 reduced the binding of hu4G4 but not hu4H12 to the B7-H3 protein, implying that hu4G4 and hu4H12 bind to different epitopes of B7-H3. Additionally, 4G4 and 4H12 specifically bound to the B7-H3 protein rather than other B7 family proteins (B7-H1, B7-H2, B7-H4, B7-H5, B7-H6, and B7-H7). These results indicate that 4G4 and 4H12 exclusively recognize membrane expression of B7-H3 in glioma cells and could be good candidate antibodies for further developing RIT for glioma.

3.2. Biological properties of the humanized anti-B7-H3 antibodies

The sequences of the VH and VL of the murine antibodies 4G4 and 4H12 were analyzed, and the complementarity-determining region (CDR) distribution of the variable domain is listed in Fig. 1(a). According to the humanness assessment, the humanized antibody residue sequence aligned with those of hu4G4 and hu4H12 (Fig. 1(b)). The humanness of the 4G4 and 4H12 variable domains (the Z score of the VH variable domain was –0.40 for 4G4 and –0.01 for 4H12, and that of the VL variable domain was –2.50 for 4G4 and –2.40 for 4H12) was lower than that of hu4G4 and hu4H12 (the Z score of the VH variable domain was –0.01 for hu4G4 and 0.30 for hu4H12, and that of the VL variable domain was –1.80 for hu4G4 and –0.90 for hu4H12). This suggested that the designed humanized antibodies hu4G4 and hu4H12 had weaker immunogenicity than the murine antibodies 4G4 and 4H12. The 3D variable domain structures of the VH and VL of the murine and humanized antibodies were modeled and optimized (Fig. 1(c)) based on computer-guided homology modeling. Main-chain carbon atom orientation superimposition was then carried out between 4G4 and hu4G4 and between 4H12 and hu4H12, and the root mean square distance (RMSD) of the main chain carbon atoms was calculated. The RMSD value of the VH variable domain was 0.00336 nm for 4G4 and 0.14970 nm for 4H12, while that of the VL variable domain was 0.00688 nm for 4G4 and 0.00317 nm for 4H12 (Fig. 1(d)).

Furthermore, the whole variable domain (i.e., Fv) conformation of the two antibodies was predicted using molecular docking to understand the structural differences in the whole variable domain between 4G4 and hu4G4 and between 4H12 and hu4H12 (Fig. 1(e)). The RMSD value of the whole variable domain main chain carbon atom was 0.01315 nm for 4G4 and 0.11530 nm for 4H12. These results suggested that the humanized antibodies hu4G4 and hu4H12 should retain the activity of 4G4 and 4H12, respectively.

Plasmids encoding humanized or original antigen-binding fragment (*Fab*) genes were transformed into XLI-Blue cells and expressed with isopropyl-β-*D*-thiogalactopyranoside (IPTG) induction in super broth (SB) medium. The expressed products were briefly purified by a SephacrylS-200 Superfine column after ammonium sulfate fractionation. The purified products were subjected to 12% sodium dodecyl sulfate–polyacrylamide gel electrophoresis (SDS-PAGE), and one obvious band of 50 kDa was observed (Fig. 2(a)). Although not superfine, the purity and yield of the Fabs were sufficient for subsequent research. The binding reactivity of hu4G4 and hu4H12 with the antigen human B7-H3 protein was tested by flow cytometry (Fig. 2(b)) and Biacore (Fig. 2(c)). The results of flow cytometry analysis suggested that hu4G4 and hu4H12 specifically recognized B7-H3 and had similar binding reactivity to the parental murine antibodies. The results of Biacore showed that 4G4/4H12 could compete with binding of hu4G4/hu4H12 to the B7-H3 protein. This means that the epitopes of the B7-H3 protein recognized by the antibodies were not changed during antibody humanization (Fig. 2(d)). To determine the forces required to separate individual Fab–antigen interactions, the Biacore system was used. The distribution of unbinding forces needed to separate the specific interaction between the antibody on the tip and the antigen on the surface was obtained by a series of specific experiments. Analysis of the force distribution data suggested that the unbinding forces between hu4G4/hu4H12 and B7-H3 were mainly on the order of 10^{-10} mol·L^{-1}, 2.625×10^{-10} mol·L^{-1} for hu4G4 and 7.543×10^{-10} mol·L^{-1} for hu4H12 (Fig. 2(c)), in line with the levels of their parental murine antibodies (1.65×10^{-10} mol·L^{-1} for 4G4 and 1.75×10^{-10} mol·L^{-1} for 4H12), although the flow histograms showed that hu4G4 and hu4H12 had slightly higher B7-H3 binding affinity and avidity than the respective parental murine versions. These results demonstrated that the humanized version retained the specificity and affinity of their parental antibodies.

3.3. ^{89}Zr-PET imaging-guided antibody screening in mice

As shown in Fig. S3 in Appendix A, ^{89}Zr-DFO-(hu4G4, hu4H12, IgG) was radiolabeled with ^{89}Zr at a radiolabeling yield of more than 95%, and the RCPs of all were >99%. The specific activity (SA) achieved for each of the ^{89}Zr-labeled antibodies was 8.33 gigabecquerel (GBq)·μmol^{-1}. The stability values of ^{89}Zr-DFO-(hu4G4,

hu4H12, IgG) in acetate buffer at room temperature and in human serum at 37 °C were greater than 90% for 168 h *in vitro*.

The results of static PET imaging at 2, 12, 24, 48, 72, 96, 120, 144, and 168 h postadministration in U87-xenografted mice are shown in Fig. 3. PET imaging in U87-xenografted mice (Figs. 3(a) and (b)) clearly showed that ^{89}Zr-DFO was localized mainly in the liver and spleen, while ^{89}Zr-free was mainly localized in the long bone joints, with less in the tumor. ^{89}Zr-DFO-(hu4G4, hu4H12, IgG) is mainly metabolized by the liver but not the urinary system. Tumor uptake of ^{89}Zr-DFO-(hu4G4, hu4H12) was significantly higher than that of ^{89}Zr-DFO-IgG during the 168 h monitoring period, and the liver uptake of ^{89}Zr-DFO-hu4G4 was lower than that of ^{89}Zr-DFO-IgG and ^{89}Zr-DFO-hu4H12.

As shown in Figs. 3(c)–(g), the left tumor uptake of ^{89}Zr-DFO-hu4G4, increased rapidly within 24 h postinjection and continually increased until reaching a peak ((20.56 ± 6.73) %ID/g) at 96 h postinjection, while that of ^{89}Zr-DFO-hu4H12 ((19.00 ± 5.69) %ID/g) and ^{89}Zr-DFO-IgG ((8.19 ± 0.10) %ID/g) peaked at 72 h postinjection. The right tumor uptake values were in line with the of left tumor uptake values. The liver uptake of ^{89}Zr-DFO-hu4H12 peaked ((19.35 ± 2.75) %ID/g) at the earliest time point and was approximately 50% higher than that of ^{89}Zr-DFO-hu4G4, and then it gradually decreased until 168 h after injection (Fig. S4(a) in Appendix A). In addition, spleen uptake was almost constant after a slow decline from 2 to 96 h after injection (Fig. S4(b) in Appendix A). Figs. S4(c) and (d) in Appendix A shows that the left/right tumor-to-liver ratio in the ^{89}Zr-DFO-hu4G4 group was significantly higher ($p < 0.001$) than that in the ^{89}Zr-DFO-(hu4H12, IgG) group at 72 and 168 h postinjection. The tumor-to-blood ratio was notably different ($p < 0.05$) between ^{89}Zr-DFO-hu4G4 and ^{89}Zr-DFO-IgG (Fig. S4(d)). These results indicate that hu4G4 has better targeting than hu4H12.

3.4. Biodistribution and PK characteristics of the ^{89}Zr-radiolabeled antibodies

The biological properties of the ^{89}Zr-radiolabeled antibodies were further evaluated by biodistribution experiments at 72 and 168 h postinjection in U87-xenografted mice (Fig. 4).

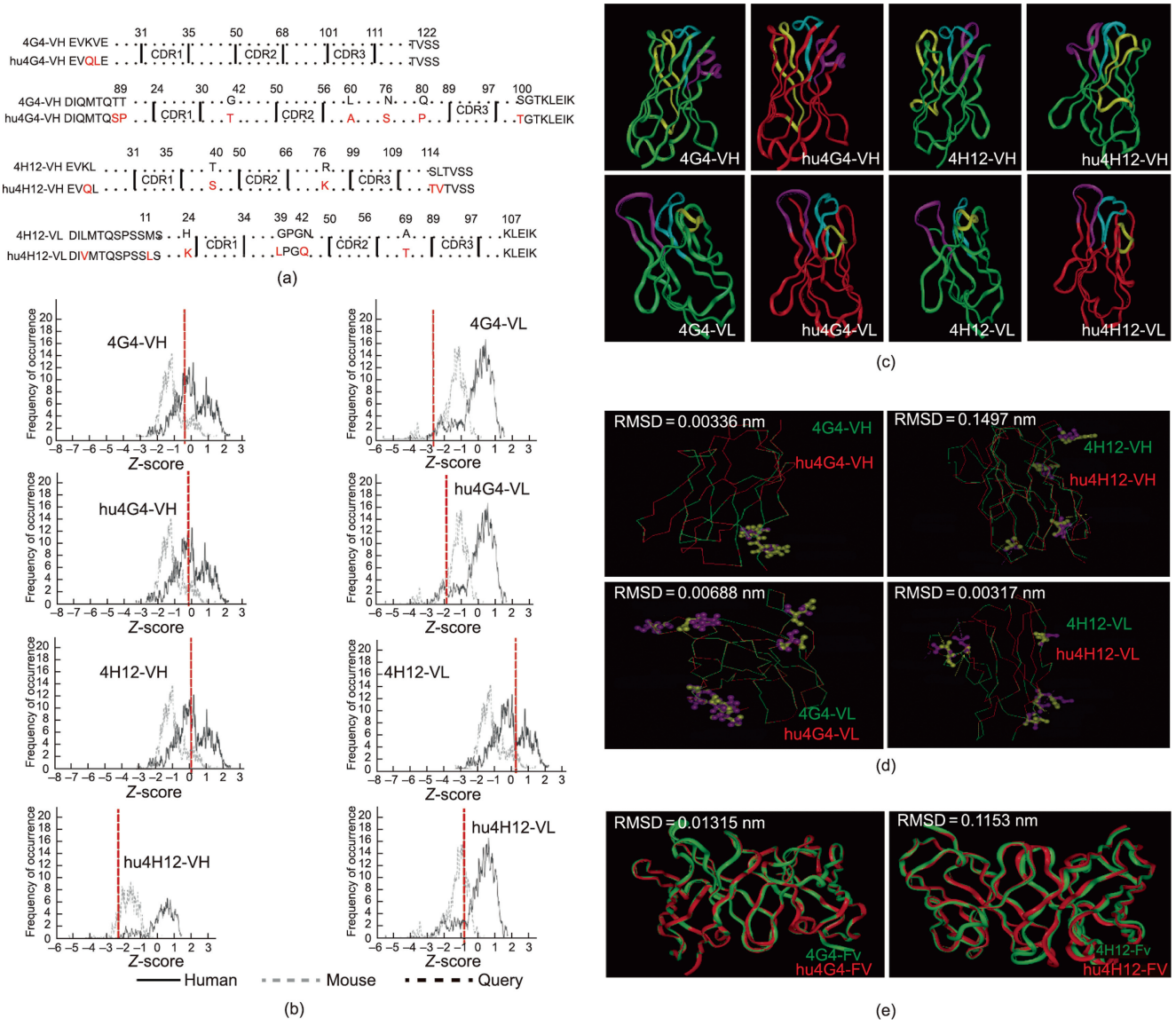

Fig. 1. Computer-aided humanization of 4G4 and 4H12. (a) Amino acid alignment of the variable domains of the humanized antibodies hu4G4 and hu4H12 and the parent murine antibodies 4G4 and 4H12. (b) Humanness analysis of the variable domains of the VH and VL of 4G4 and 4H12. (c) Modeled structures of the variable domains of 4G4 and hu4G4 and of 4H12 and hu4H12, and superimposition of the antibody chains. (d) Superimposition of the VH and VL variable domains. (e) Superimposition of the variable domains (Fv) of 4G4 and hu4G4 and of 4H12 and hu4H12.

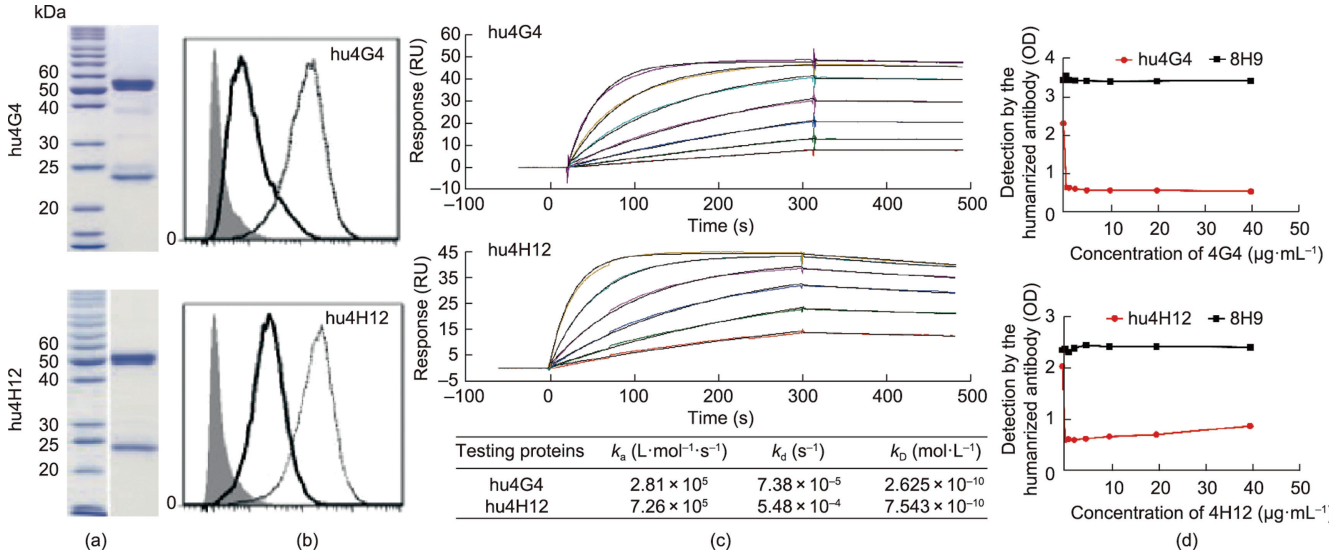

Fig. 2. Purification of hu4G4 and hu4H12 and their binding to the B7-H3 protein. (a) Analysis of Fab products by nonreducing 12% SDS-PAGE. (b) Binding of hu4G4 and hu4H12 with B7-H3 protein expressed on the surface of U87 cells. The filled histograms represent isotype controls, while the open histograms with black lines represent the 4G4 or 4H12 groups, and the dashed lines represent the hu4G4 or hu4H12 groups. (c) Kinetic analysis of antibody (hu4G4/hu4H12) binding to B7-H3 measured by Biacore. k_a: association rate constant, unit: L·mol^{-1}·s^{-1}, governs the rate at which a complex is formed; k_d: dissociation rate constant, unit: s^{-1}, governs the rate at which a complex dissociates; k_D: equilibrium dissociation constant, unit: mol·L^{-1}, describes the strength of the interaction. (d) Assessment of whether the binding epitopes of the B7-H3 protein recognized by hu4G4 and hu4H12 are different from those of their parental murine antibodies. B7-H3 protein was first incubated with 4G4 or 4H12 at increasing concentrations and then detected by hu4G4, hu4H12, or the control antibody 8H9, which recognize different epitopes than 4G4 and 4H12. RU: resonance unit; OD: optical density.

The tumor uptake in the ^{89}Zr-DFO-(hu4G4, hu4H12) groups was higher than that in the ^{89}Zr-DFO-IgG and ^{89}Zr-DFO groups, while ^{89}Zr-free was mainly concentrated in bone and long bone joints at the two time points (Figs. 4(a) and (b)). Furthermore, the tumor-to-background ratio of each group was analyzed, as shown in Figs. 4(c) and (d). The tumor-to-blood ratios in the ^{89}Zr-DFO-(hu4G4, hu4H12) groups were increased. Moreover, the left and right tumor-to-liver ratios (9.81 ± 3.69, 7.83 ± 2.46) of the ^{89}Zr-DFO-hu4G4 group were higher than those of the ^{89}Zr-DFO-hu4H12 group (3.78 ± 2.65, 2.03 ± 0.80) and the ^{89}Zr-DFO-IgG group (1.28 ± 0.47, 1.18 ± 0.40) at 72 h postinjection. At 168 h postinjection, the left/right tumor-to-liver ratio in the ^{89}Zr-DFO-hu4G4 treated group was remarkably higher ($p < 0.05$) than that in the ^{89}Zr-DFO-hu4H12 treated group. These results were consistent with the PET imaging results.

The blood uptake over time curve of ^{89}Zr-labeled antibodies in U87-xenografted mice is shown in Fig. 5. The blood uptake of ^{89}Zr-DFO-(hu4G4, hu4H12, IgG) at 30 min reached (22.20 ± 3.01), (20.87 ± 7.41), and (24.84 ± 7.54) %ID/g and then gradually decreased to stable values of (1.30 ± 1.01), (1.47 ± 0.55), and (4.81 ± 1.48) %ID/g at 168 h, respectively (Fig. 5(a)). The mean half-life ($T_{1/2}$) of ^{89}Zr-DFO-(hu4G4, hu4H12, IgG) in U87-xenografted mice was (41.72 ± 10.35), (49.61 ± 17.28), and (69.42 ± 14.24) h, respectively (Fig. 5(b)). The area under the curve (AUC) analysis confirmed that the blood exposure of ^{89}Zr-DFO-(hu4G4, hu4H12) in the blood was lower than that of ^{89}Zr-DFO-IgG (Fig. 5(c)).

3.5. SPECT imaging and biodistribution analyses of the ^{125}I-antibodies

A series of SPECT images taken at 24, 48, and 72 h are presented in Fig. 6(a). The ratios of tumor to organs were calculated by ROI analysis of the SPECT images (Fig. 6(b)). The tumor-to-blood ratio for ^{125}I-hu4G4 was significantly higher than that for ^{125}I-IgG ($p < 0.05$) and that for ^{125}I-hu4H12 ($p < 0.01$). This trend was consistent with the tumor-to-muscle and tumor-to-liver ratios, indicating that hu4G4 had higher tumor targeting with lower liver uptake and faster blood clearance. The biodistribution results of the ^{125}I-labeled antibody (Fig. 6(c)) were consistent with the SPECT imaging results. In addition, high physiological uptake of radioiodine was found in the liver and thyroid glands.

3.6. Dosimetry

As shown in Fig. S5 in Appendix A, the tumor absorbed doses in the ^{131}I-(IgG, hu4G4, hu4H12) group, which were calculated based on the ^{125}I-SPECT images, were (1.92 ± 0.27), (4.85 ± 0.67), and (3.84 ± 1.02) mGy·MBq^{-1}, respectively, while that in the ^{131}I-IgG group was (1.83 ± 0.53) mGy·MBq^{-1}. The tumor absorbed dose of ^{131}I-hu4G4 was higher ($p < 0.05$) than that of ^{131}I-IgG or Na^{131}I, while there was no notable difference between the tumor absorbed doses of ^{131}I-hu4G4 and ^{131}I-hu4H12.

3.7. Antitumor efficacy and decreased toxicity of ^{131}I-hu4G4 radiotherapy in U87-xenografted mice

The radiochemical yield of ^{131}I-hu4G4 was more than 95%, and the RCP was > 99% according to both radio-TLC and HPLC analyses (Figs. S6 and S7 in Appendix A). The SA was calculated to be 55.5 GBq·μmol^{-1}. ^{131}I-hu4G4 showed ideal stability *in vitro* after incubation in PBS and serum for 168 h (Fig. S6).

A schematic diagram of the PD analysis of ^{131}I-hu4G4 in U87-xenografted mice is shown in Fig. 7(a). During the treatment period, ^{131}I-hu4G4 had remarkable treatment efficacy, and the tumor volumes in the treated group were significantly smaller than those of PBS-treated mice ($p < 0.001$) and hu4G4-treated mice ($p < 0.001$) at days 21 postinjection (Figs. 7(b)–(d)). The tumor weights in the ^{131}I-hu4G4 group were also smaller ($p < 0.001$) than those in the PBS and hu4G4 groups, but there was no significant difference compared to the ^{131}I-IgG treated group at days 21 postinjection as shown in Fig. 7(e). Furthermore, the tumor relative growth rate (%T/C) was analyzed, as shown in Fig. 7(f). The slope in the ^{131}I-hu4G4 group decreased rapidly and reached 40% within 10 d of treatment. On day 21, the tumor growth inhibition rate (%TGI) of

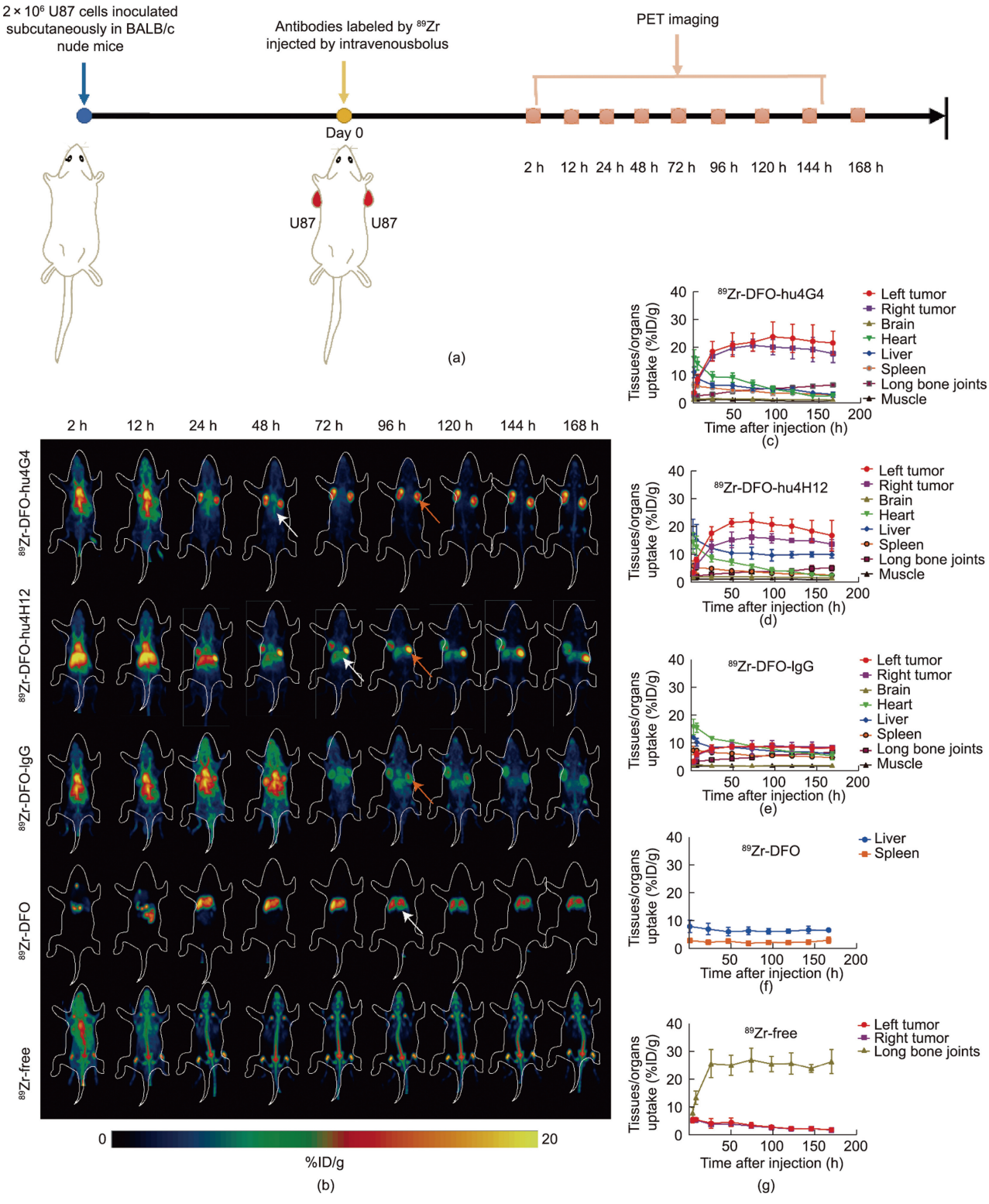

Fig. 3. B7-H3-targeted antibody screening with ^{89}Zr-immunoPET imaging in U87-xenografted mice. (a) Schematic approach by ^{89}Zr-immunoPET imaging. (b) Representative maximum intensity projections (MIPs) determined by PET imaging of ^{89}Zr-labeled antibodies at different time points in each group after intravenous injection (n = 6). (c)–(g) Time-radioactivity curves of tissues or organs (left tumor, right tumor, brain, heart, liver, spleen, and long bone joints) in each group (n = 6). The orange arrow denotes the tumor. The white arrow indicates the liver.

^{131}I-hu4G4 was 68.47%, while that of ^{131}I-IgG was 53.28% (Table S1 in Appendix A). In addition, the inhibition of tumor growth in mice in the ^{131}I-hu4G4 group led to a corresponding increase in survival, which was longer than that of mice in any other group (Fig. 7(g)).

^{18}F-FDG PET imaging was performed according to the schematic diagram (Fig. 8(a)). The baseline ^{18}F-FDG uptake was obtained by PET scans in tumors before treatment, followed by ^{18}F-FDG PET scans after treatment for 7 d (Fig. 8(b)). We found that ^{18}F-FDG

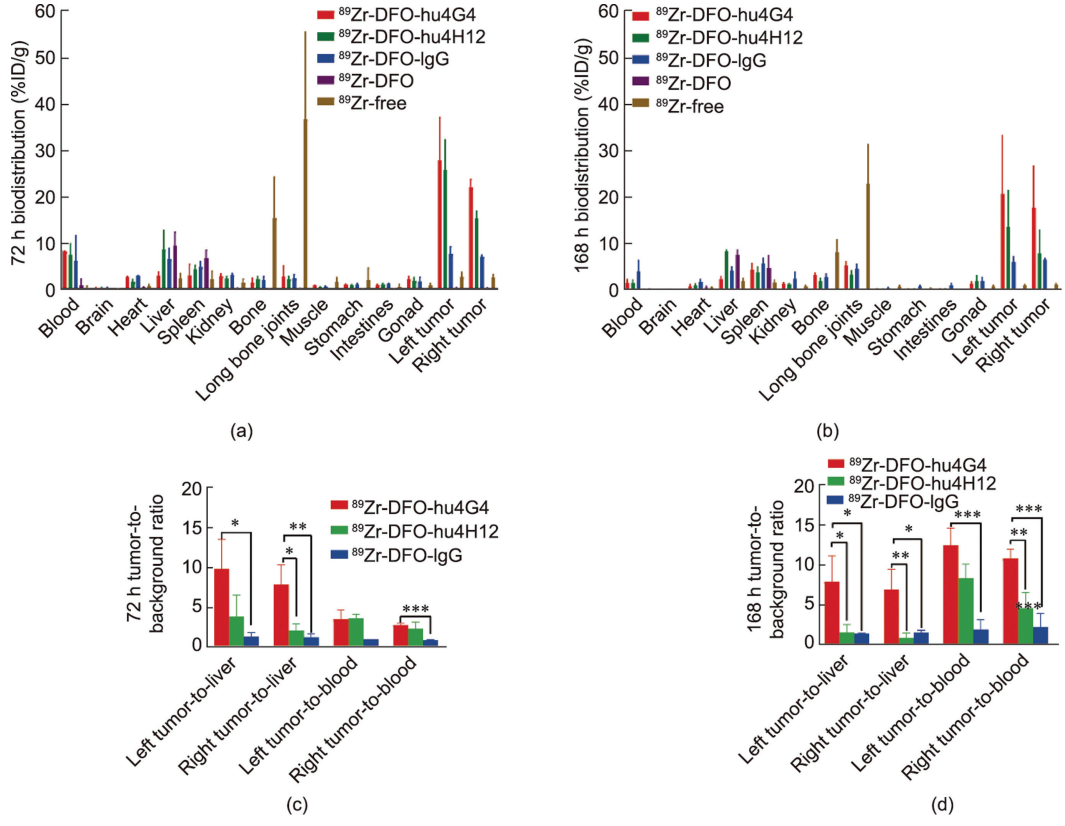

Fig. 4. *Ex vivo* biodistribution of ^{89}Zr-labeled antibodies in U87-xenografted mice. Biodistribution of ^{89}Zr-labeled antibody at (a) 72 and (b) 168 h postadministration. Target-to-background ratios of ^{89}Zr-DFO-antibodies (hu4G4, hu4H12, or IgG) determined by *ex vivo* biodistribution at (c) 72 and (d) 168 h postinjection in U87-xenografted mice (n = 4).

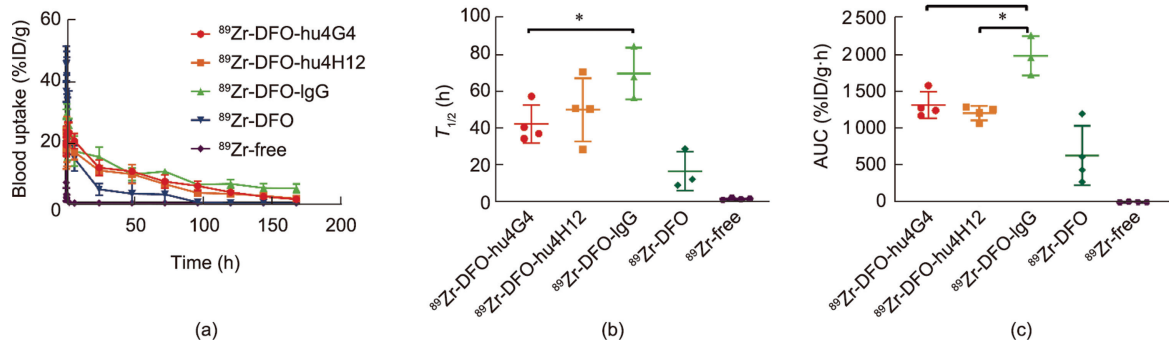

Fig. 5. PK characteristics in U87-xenografted mice. (a) Time-activity curves of ^{89}Zr-labeled antibodies in blood at various time points within 168 h postinjection. The results of (b) mean half-life ($T_{1/2}$) and (c) AUC for the blood uptake.

uptake in tumors was nearly identical in each group at baseline, while after 7 d of treatment, the tumor uptake in the ^{131}I-hu4G4 group ((7.58 ± 1.29) %ID/g) was lower than that in the PBS group ((9.70 ± 1.67) %ID/g, $p < 0.05$) or the hu4G4 group ((9.94 ± 1.23) %ID/g, $p < 0.05$) (Fig. 8(c)). These results show that the ^{131}I-hu4G4 group had the slowest glucose metabolism of all the groups, which was consistent with the tumor relative growth rate (%T/C) results at 21 d after treatment.

The safety of ^{131}I-(hu4G4, IgG) was assessed in various experiments over the course of the study. Body weight was monitored every two days to check for systemic toxicity (Fig. S8(a) in Appendix A). To assess heme toxicity, complete blood count analyses were performed at various time points in the ^{131}I-hu4G4 group (Figs. S8(b)–(d) in Appendix A). Notably, red blood cell platelet counts in mice fluctuated within the normal range (Figs. S8(b) and (d)). However, white blood counts were already above average levels before treatment (Fig. S8(c)). This was partly due to inflammation. During treatment, the white blood counts of mice transiently decreased and then gradually increased as a result of resulting from inflammation increasing during treatment.

Most mice in the groups were near their original pretherapy weight at the time they were sacrificed. In addition, no heart, liver, spleen, lung, and kidney morphology abnormalities were observed at day 7 or day 21 by H&E staining in each group (Fig. 9).

3.8. ^{131}I-hu4G4 improves tumor vascular structure in tissues with higher expression of Col IV and PDGFR-β

To study the effect of ^{131}I-hu4G4 on tumor vessel structure and morphology, tumor tissues were collected from the mice at the last

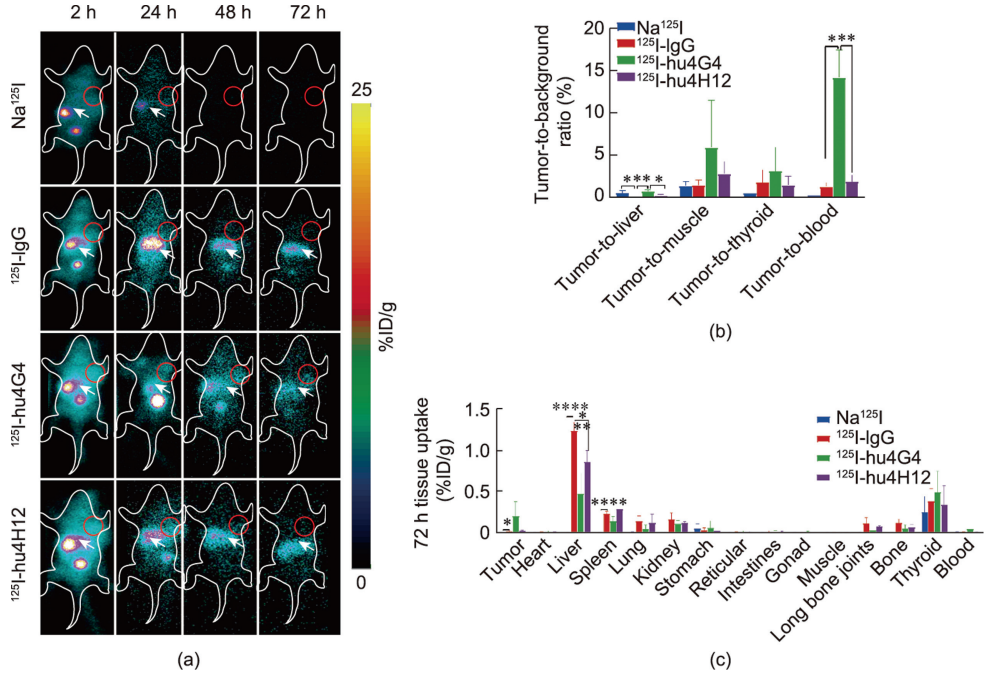

Fig. 6. B7-H3-targeted antibody screening with ^{125}I-SPECT imaging in U87-xenografted mice. (a) The MIPs derived from SPECT imaging at different time points in each group after injection (n = 5). (b) Tumor-to-background ratio of the ^{125}I-hu4G4 group at 24 h based on uptake in ROIs of the images. (c) *Ex vivo* biodistribution of ^{125}I-hu4G4 in U87-xenografted mice at 72 h postadministration. The red circle denotes the tumor. The white arrow indicates the liver.

time point during treatment. We investigated the expression of PDGFR-β (a marker of pericyte (PC) coverage) and Col IV basement membrane (BM) coverage in tumor vessels by IF staining (Fig. 10(a)). CD31 (a panendothelial cell marker), PDGFR-β/Col IV, and DAPI were used for triple staining.

We observed scarce expression of CD31 and PDGFR-β in the PBS group (Figs. 10(b) and (c)). Remarkably, in our investigations of the structural and functional alterations of blood vessels in the tumor core region, ^{131}I-hu4G4 enhanced blood vascular (BV) density (four-fold) (Fig. 10(b)), PDGFR-β PC coverage on tumor vessels (four-fold) (Fig. 10(d)), and Col IV^{+} BM coverage (six-fold) (Fig. 10(c)) in tumor vasculature compared with PBS. However, Col IV and PDGFR-β staining was almost never observed in the PBS-treated group. This could be because the tumor tissue appeared necrotic in the PBS-treated group. In addition, the BV density (%) and BM coverage (%) in the ^{131}I-IgG group were remarkably lower than those in the ^{131}I-hu4G4 group. There was no significant difference between the ^{131}I-IgG and ^{131}I-hu4G4 groups in the PC coverage (%).

3.9. Preliminary assessment of the antitumor efficacy of ^{131}I-hu4G4 radiotherapy in a in situ glioma tumor model

As shown in Fig. S9 in Appendix A, we verified the efficacy of ^{131}I-hu4G4 in orthotopic glioma tumors. As expected, the therapeutic efficacy of ^{131}I-hu4G4 was better than that of PBS (p < 0.05) in the *in situ* glioma tumor model. The survival rate in the ^{131}I-hu4G group was 75.0%, while the survival rate in the PBS group was 37.5%. During treatment, the body weights of the ^{131}I-hu4G4 and control groups slightly decreased.

4. Discussion

RIT, which has advantages in treating localized, metastatic, diffuse, and occult disease, has been in the spotlight in the targeted treatment for cancer [28]. However, antibody selection and design are critical to RIT. An ideal antibody should have high affinity for the target antigen, minimal binding to nonmalignant tissue, the ability to rapidly and uniformly penetrate tumor nodules, and rapid clearance from the blood circulation immediately after maximal tumor binding is achieved to prevent exposure of normal tissues and organs (such as liver, kidney, bone marrow, and other major organs) to radioactivity [6].

In this paper, we developed two specific anti-B7-H3 humanized antibodies, hu4G4 and hu4H12, with potential therapeutic properties and radiolabeled them with ^{89}Zr with a high yield (> 95%), high RCP (> 99%), and good *in vitro* stability (≥ 90%) after 168 h of incubation in acetate buffer or plasma, providing the basis for further biological evaluations.

In the investigation of the targeting efficiency and specificity of the antibodies, PET imaging showed high and specific accumulation of ^{89}Zr-DFO-(hu4G4, hu4H12) in U87 tumor lesions but very low uptake of ^{89}Zr-DFO-IgG, possibly due to Fc-mediated uptake of IgG. This is in agreement with the preclinical results previously reported by Burvenich et al. [29]. Nonspecific uptake in normal organs, mainly liver and kidney, is also used for toxicity assessment as an indicator of RIT antibody performance. As shown in Fig. S4(a), the liver uptake in each group at 168 h postinjection was as follows: ^{89}Zr-DFO-hu4G4 ((2.84 ± 0.95) %ID/g) < ^{89}Zr-DFO-IgG ((5.305 ± 0.18) %ID/g) < ^{89}Zr-DFO-hu4H12 ((10.23 ± 0.06) %ID/g). We speculated that the liver may be the main metabolic organ of ^{89}Zr-DFO-(hu4G4, hu4H12, IgG), which is consistent with the results published by Wu [30]. To further verify the *in vivo* biological behavior of the antibody, SPECT imaging with ^{125}I-labeled antibodies was conducted. Consistent with other studies, although the same precursor antibodies were radiolabeled, the distribution results from ^{125}I-SPECT imaging and ^{89}Zr-PET imaging were not identical, especially regarding distribution in the thyroid gland and long bone joints which may be related to the *in vivo* stability of the radiolabeled antibodies and the biological behavior of the free nuclide. Nevertheless, the concentration trends in the tumor and liver were largely consistent between these two methods. All these results suggest that hu4G4 may be a more suitable candidate antibody for RIT compared than hu4H12.

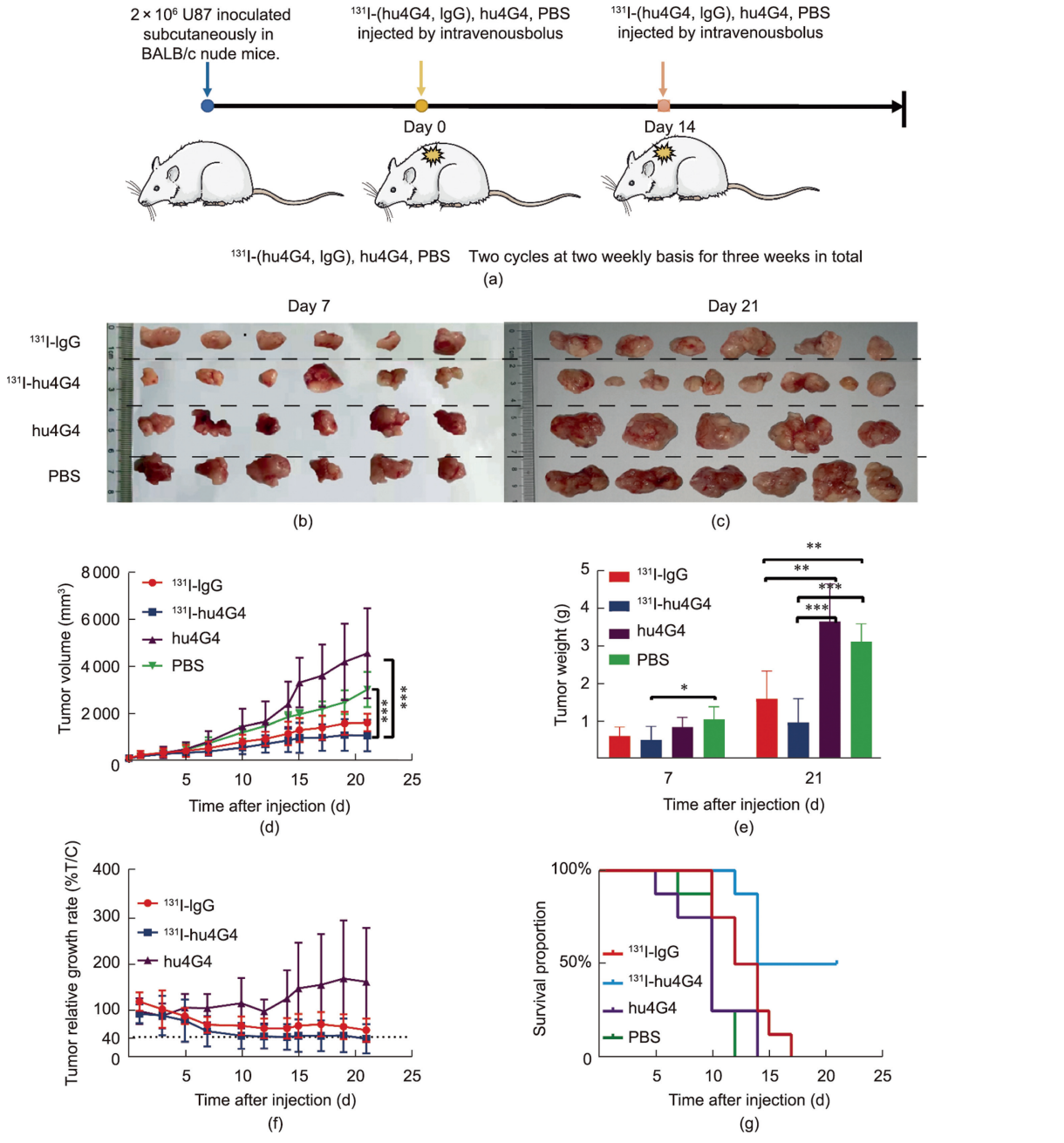

Fig. 7. PD characteristics of ^{131}I-hu4G4 in U87-xenografted mice. (a) Schematic of the treatment approach. Images of tumors (b) 7 and (c) 21 d postinjection, respectively. (d) Growth of subcutaneous tumors within 21 d. (e) Tumor weight at 7 and 21 d postinjection. (f) Tumor relative growth rate (%T/C) curve. (g) Survival proportion curve.

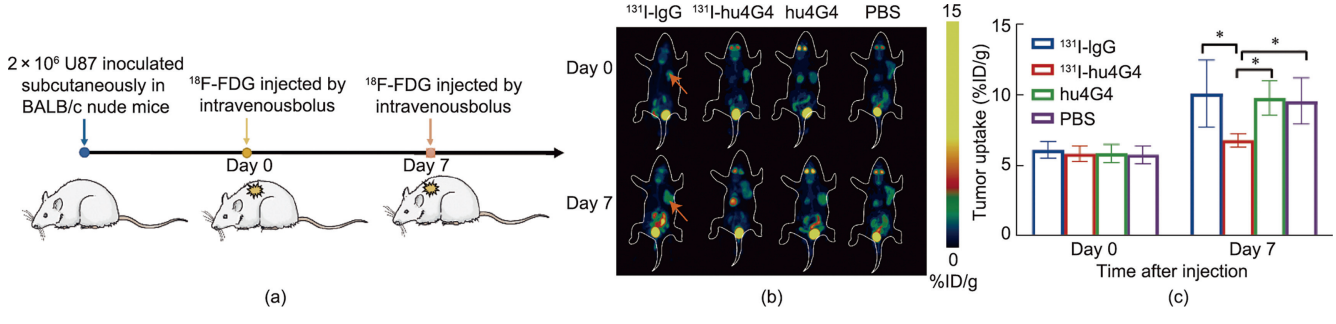

Fig. 8. Evaluation of early therapeutic efficacy by ^{18}F-FDG PET. (a) Schematic of ^{18}F-FDG PET imaging. (b) Representative MIPs determined by PET imaging of ^{18}F-FDG at days 0 and 7 after injection. (c) Tumor uptake of ^{18}F-FDG after injection at two time points. The orange arrow indicates the tumor.

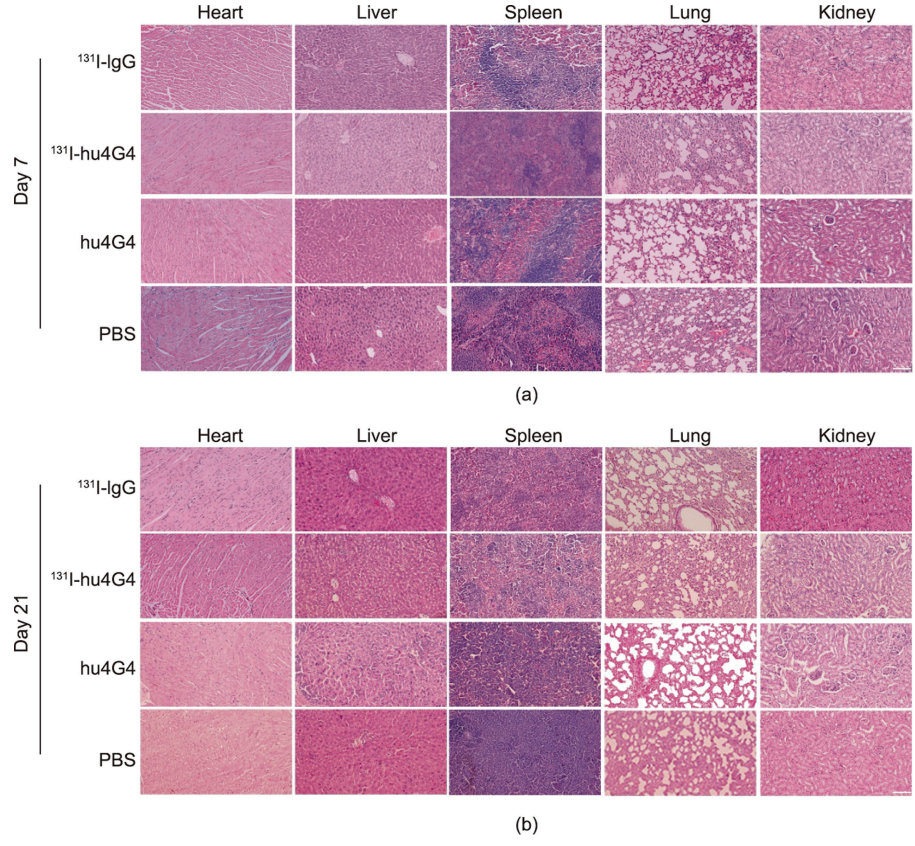

Fig. 9. Safety assessment of each group. H&E staining of tissues sections (heart, liver, spleen, lung, and kidney) at (a) days 7 and (b) 21 after injection, respectively. Scale bars: 200 μm.

Furthermore, we also established a U87 subcutaneous xenograft model and GL261 Red-FLuc-B7-H3 *in situ* glioma tumor model to test the therapeutic efficacy of hu4G4 for RIT. ^{131}I-hu4G4 was used for the preliminary *in vivo* therapeutic efficacy assessment. The PD assessment showed that the ^{131}I-hu4G4 group had a significantly reduced tumor volume (Figs. 7(b)–(d)), with the highest %TGI (down to 68.47%) (Table S1), compared with the ^{131}I-IgG, unlabeled hu4G4, and PBS groups. This therapeutic efficacy was related to radioactive uptake in tumors (Figs. S10(a) and (b) in Appendix A). The higher tumor uptake in the ^{131}I-hu4G4 group resulted in an approximate dose of (0.055 ± 0.008) Gy, while the lower tumor uptake in the ^{131}I-IgG group resulted in an accordingly lower dose of (0.023 ± 0.003) Gy. *Ex vivo* biodistribution showed that the tumor uptake of ^{131}I-hu4G4 was approximately ten-fold higher than that of the other groups at day 7 after treatment (Figs. S10 (c) and (d) in Appendix A). Simultaneously, the tumor-to-liver and tumor-to-muscle ratios of the ^{131}I-hu4G4 group were significantly higher than those of the other groups at day 21 after the second administration. However, there were no significant differences in the therapeutic benefit between mice treated with ^{131}I-hu4G4 vs ^{131}I-IgG. This phenomenon may have occurred due to for two reasons: there were individual differences in tumor volume among the animal models in each group; there is a correlation between initial tumor size and curability with uniformly targeted therapy with beta-emitting radionuclides. O'Donoghue et al. [31] reported that when the diameter of a tumor was 2.6–5.0 mm, ^{131}I could produce a maximum cure probability of 0.9. The most important mechanism is an increase in clonogenic cells, which causes the chance for tumor cure to decrease as the tumor grows. These results were also confirmed by Gaze et al. [32].

Early efficacy assessment is important for the rational use of drugs for cancer patients [33]. We used ^{18}F-FDG PET imaging to predict the treatment response before measuring the tumor size in U87-xenografted mice and found that ^{131}I-hu4G4 RIT markedly attenuated glucose metabolism (Figs. 8(b) and (c)) before the tumor volume changed. These data suggest that ^{18}F-FDG PET imaging could be useful for monitoring early therapeutic efficacy in B7-H3-targeted RIT.

Klug et al. [34] reported that local low-dose irradiation programs normalize aberrant vasculature and confirmed that the structure and function of the blood vessels could be changed and improved. We found that ^{131}I-hu4G4 improved the tumor vascular structure in tissues with higher expression of Col IV and PDGFR-β compared with the control treatment. Successful recruitment and proper coverage of PCs is important for the integrity of mature vessel structures, reducing leakiness and improving perfusion. The expression of CD31 and PDGFR-β in the tumor vasculature in the ^{131}I-hu4G4-treated group was higher than that in the ^{131}I-IgG and PBS groups, suggesting that more PCs were recruited to mature blood vessels formed in the ^{131}I-hu4G4 group. This phenomenon was also observed after co-staining to detect Col IV BM coverage and CD31 cells. However, PDGFR-β and Col IV showed almost no expression in the PBS group, which may be because the tumor volume was so large that the tumor tissue appeared necrotic, and the lower expression in the ^{131}I-IgG group was due to the following reasons: the nonspecific tumoral uptake of isotype control antibody may have been driven by the IgG1–Fc interaction [35]; the antibody may have accumulated selectively in tumors because of their leaky vasculature, which enhanced the permeability and retention of the antibodies in this compartment [36,37]; and ^{131}I may have passively accumulated in tumor tissues expressing sodium/iodide symporter [38–40].

However, some limitations exist in the study. First, we studied the preliminary efficacy of ^{131}I-hu4G4 radiotherapy in the *in situ*

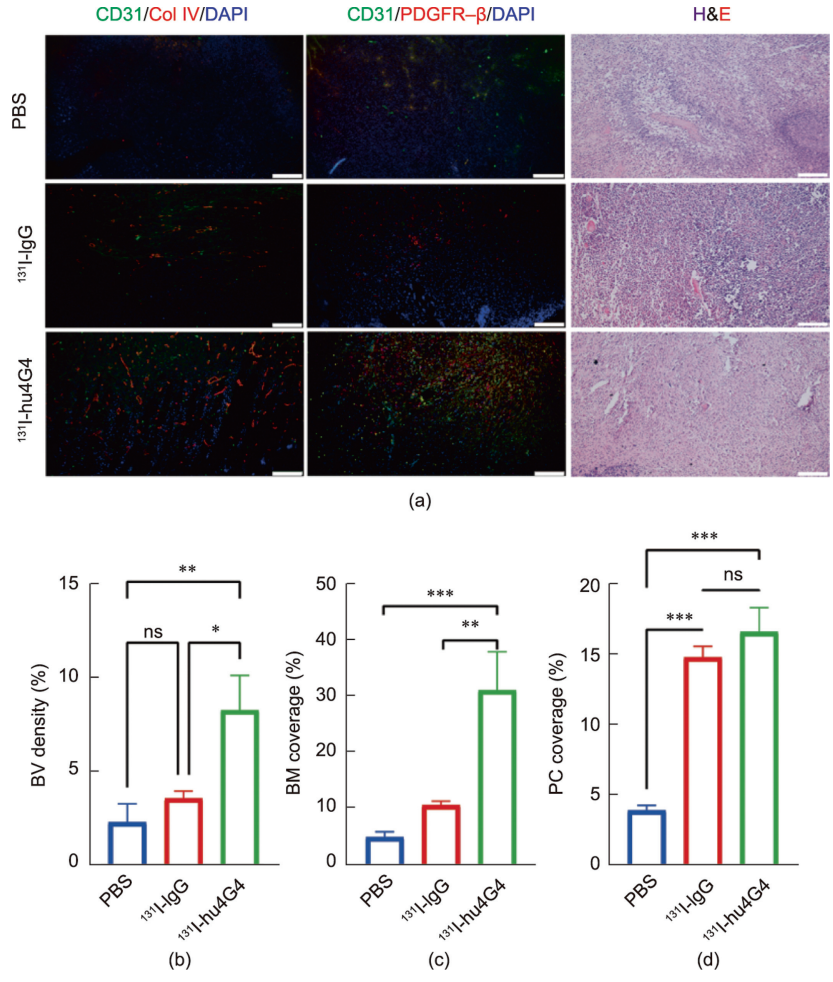

Fig. 10. ^{131}I-hu4G4 improved the tumor vascular structure in tissues with higher expression of Col IV and PDGFR-β. (a) Representative images of IF and H&E staining in each group. (b) The blood vascular (BV) density in U87 tumor tissue sections was analyzed based on CD31 (green) IF staining. (c) The BM coverage in U87 tumor tissue sections was analyzed based on Col IV (red), CD31 (green), and DAPI (blue) IF staining. The PC coverage in U87 tumor tissue sections was analyzed based on PDGFR-β (red), CD31 (green), and DAPI (blue) IF staining. The morphology of tumor tissues was assessed by H&E staining. Scale bars: 200 μm. BV density (%), BM coverage (%), and PC coverage (%) are presented as the mean fluorescence density. ns: no significance.

glioma tumor model, but further in-depth research is still needed. In addition, the radioactive administered dose (i.e., administered activity) and the mass dose of a pharmaceutical are two vital factors that need to be considered for RIT. Therefore, more studies are needed to determine the administration schedule for ultimate clinical translation. Finally, our work preliminarily revealed that ^{131}I-hu4G4 improved the tumor vessel structure, but the antitumor mechanism of ^{131}I-hu4G4 needs to be further explored.

In conclusion, we found that the B7-H3-targeted humanized antibody hu4G4 is a candidate antibody for RIT with excellent tumor targeting and specificity, and it demonstrated higher tumor uptake with low nonspecific concentrations in normal tissues, especially in the liver. ^{131}I-hu4G4 showed promising antitumor efficacy, inducing multiple pathologically confirmed complete responses and minimal apparent toxicity. ^{131}I-hu4G4 could be a promising agent for further preclinical studies of glioma treatment.

Acknowledgments

This work was funded by the National Natural Science Foundation of China (31320103918 and 82104318); Key Research and Development Program of Jiangsu Province (BE2021644); the Jiangsu Innovative and Entrepreneurial Talent Programme (JSSCBS20211568); the Science and Technology Plan of Suzhou (SKJYD2021161 and SKY2022046); Key Project of Jiangsu Provincial Health Commission (zd2021050); and the Project of State Key Laboratory of Radiation Medicine and Protection, Soochow University (GZK1202203). We also appreciate the support of Jiangsu Institute of Nuclear Medicine for the ^{89}Zr-PET imaging in this study.

Authors' contribution

Fengqing Fu, Meng Zhengand, and Shandong Zhao performed all the experiments and wrote the manuscript. Yan Wang analyzed the data. Minzhou Huang and Kaijie Zhang performed some of the experiments. Hanqing Chen and Ziyi Huang helped with the antibody humanization. Xueguang Zhang and Liyan Miao conceptualized the research and revised the manuscript. All authors reviewed the manuscript.

Compliance with ethics guidelines

Fengqing Fu, Meng Zheng, Shandong Zhao, Yan Wang, Minzhou Huang, Hanqing Chen, Ziyi Huang, Kaijie Zhang, Liyan Miao, and Xueguang Zhang declare that they have no conflicts of interest or financial conflicts to disclose.

Appendix A. Supplementary data

Supplementary data to this article can be found online at https://doi.org/10.1016/j.eng.2023.05.011.

References

[1] Gaspar LE, Fisher BJ, Macdonald DR, Leber DV, Halperin EC, Schold SC, et al. Supratentorial malignant glioma: patterns of recurrence and implications for external beam local treatment. Int J Radiat Oncol Biol Phys 1992;24(1):55–7.

[2] Ostrom QT, Patil N, Cioffi G, Waite K, Kruchko C, Barnholtz-Sloan JS. CBTRUS statistical report: primary brain and other central nervous system tumors diagnosed in the United States in 2013–2017. Neuro-oncol 2020;22(12 Suppl 2):iv1–96.

[3] Reardon DA, Zalutsky MR, Bigner DD. Antitenascin-C monoclonal antibody radioimmunotherapy for malignant glioma patients. Expert Rev Anticancer Ther 2007;7(5):675–87.

[4] Bleeker FE, Molenaar RJ, Leenstra S. Recent advances in the molecular understanding of glioblastoma. J Neurooncol 2012;108(1):11–27.

[5] Xu S, Tang L, Li X, Fan F, Liu Z. Immunotherapy for glioma: current management and future application. Cancer Lett 2020;476:1–12.

[6] Larson SM, Carrasquillo JA, Cheung NKV, Press OW. Radioimmunotherapy of human tumours. Nat Rev Cancer 2015;15(6):347–60.

[7] Pouget JP, Navarro-Teulon I, Bardiès M, Chouin N, Cartron G, Pèlegrin A, et al. Clinical radioimmunotherapy—the role of radiobiology. Nat Rev Clin Oncol 2011;8(12):720–34.

[8] Bischof DA. The role of nuclear medicine in the treatment of non-Hodgkin's lymphoma (NHL). Leuk Lymphoma 2003;44(Suppl 4):S29–36.

[9] Yudistiro R, Hanaoka H, Katsumata N, Yamaguchi A, Tsushima Y. Bevacizumab radioimmunotherapy (RIT) with accelerated blood clearance using the avidin chase. Mol Pharm 2018;15(6):2165–73.

[10] Sugyo A, Tsuji AB, Sudo H, Okada M, Koizumi M, Satoh H, et al. Evaluation of efficacy of radioimmunotherapy with ^{90}Y-labeled fully human anti-transferrin receptor monoclonal antibody in pancreatic cancer mouse models. PLoS One 2015;10(4):e0123761.

[11] Fujiwara K, Koyama K, Suga K, Ikemura M, Saito Y, Hino A, et al. ^{90}Y-labeled anti-ROBO1 monoclonal antibody exhibits antitumor activity against small cell lung cancer xenografts. PLoS One 2015;10(5):e0125468.

[12] Herrmann K, Schwaiger M, Lewis JS, Solomon SB, McNeil BJ, Baumann M, et al. Radiotheranostics: a roadmap for future development. Lancet Oncol 2020;21(3):e146–56.

[13] Hofmeyer KA, Ray A, Zang X. The contrasting role of B7-H3. Proc Natl Acad Sci USA 2008;105(30):10277–8.

[14] Seaman S, Stevens J, Yang MY, Logsdon D, Graff-Cherry C, St CB. Genes that distinguish physiological and pathological angiogenesis. Cancer Cell 2007;11(6):539–54.

[15] Zhong C, Tao B, Chen Y, Guo Z, Yang X, Peng L, et al. B7-H3 regulates glioma growth and cell invasion through a JAK2/STAT3/Slug-dependent signaling pathway. OncoTargets Ther 2020;13:2215–24.

[16] Wang Z, Wang Z, Zhang C, Liu X, Li G, Liu S, et al. Genetic and clinical characterization of B7-H3 (CD276) expression and epigenetic regulation in diffuse brain glioma. Cancer Sci 2018;109(9):2697–705.

[17] Jackson CM, Choi J, Lim M. Mechanisms of immunotherapy resistance: lessons from glioblastoma. Nat Immunol 2019;20(9):1100–9.

[18] Kaplon H, Muralidharan M, Schneider Z, Reichert JM. Antibodies to watch in 2020. MAbs 2020;12(1):1703531.

[19] Kramer K, Kushner BH, Modak S, Pandit-Taskar N, Smith-Jones P, Zanzonico P, et al. Compartmental intrathecal radioimmunotherapy: results for treatment for metastatic CNS neuroblastoma. J Neurooncol 2010;97(3):409–18.

[20] Wang Y, Pan D, Huang C, Chen B, Li M, Zhou S, et al. Dose escalation PET imaging for safety and effective therapy dose optimization of a bispecific antibody. MAbs 2020;12(1):1748322.

[21] Ehlerding EB, Lacognata S, Jiang D, Ferreira CA, Goel S, Hernandez R, et al. Targeting angiogenesis for radioimmunotherapy with a ^{177}Lu-labeled antibody. Eur J Nucl Med Mol Imaging 2018;45(1):123–31.

[22] Lopci E, Chiti A, Castellani MR, Pepe G, Antunovic L, Fanti S, et al. Matched pairs dosimetry: ^{12}4I/^{13}1I metaiodobenzylguanidine and ^{12}4I/^{13}1I and ^{8}6Y/^{9}0Y antibodies. Eur J Nucl Med Mol Imaging 2011;38(Suppl 1):S28–40.

[23] Stabin MG, Sparks RB, Crowe E. OLINDA/EXM: the second-generation personal computer software for internal dose assessment in nuclear medicine. J Nucl Med 2005;46(6):1023–7.

[24] Tully KM, Tendler S, Carter LM, Sharma SK, Samuels ZV, Mandleywala K, et al. Radioimmunotherapy targeting delta-like ligand 3 in small cell lung cancer exhibits antitumor efficacy with low toxicity. Clin Cancer Res 2022;28(7):1391–401.

[25] Fu F, Gao J, Chen H, Wang W, Sun J, Zhang X et al. Downregulated miR-339-5p leads to overexpression of B7-H3 on glioma with tumor progression and invasion. Int J Biol Res. In press.

[26] Modak S, Kramer K, Gultekin SH, Guo HF, Cheung NK. Monoclonal antibody 8H9 targets a novel cell surface antigen expressed by a wide spectrum of human solid tumors. Cancer Res 2001;61(10):4048–54.

[27] Lemke D, Pfenning PN, Sahm F, Klein AC, Kempf T, Warnken U, et al. Costimulatory protein 4IgB7H3 drives the malignant phenotype of glioblastoma by mediating immune escape and invasiveness. Clin Cancer Res 2012;18(1):105–17.

[28] Vassileva V, Rajkumar V, Mazzantini M, Robson M, Badar A, Sharma S, et al. Significant therapeutic efficacy with combined radioimmunotherapy and cetuximab in preclinical models of colorectal cancer. J Nucl Med 2015;56(8):1239–45.

[29] Burvenich IJG, Parakh S, Lee FT, Guo N, Liu Z, Gan HK, et al. Molecular imaging of T cell co-regulator factor B7-H3 with ^{89}Zr-DS-5573a. Theranostics 2018;8(15):4199–209.

[30] Wu AM. Engineered antibodies for molecular imaging of cancer. Methods 2014;65(1):139–47.

[31] O'Donoghue JA, Bardiès M, Wheldon TE. Relationships between tumor size and curability for uniformly targeted therapy with beta-emitting radionuclides. J Nucl Med 1995;36(10):1902–9.

[32] Gaze MN, Mairs RJ, Boyack SM, Wheldon TE, Barrett A. ^{131}I-meta-iodobenzylguanidine therapy in neuroblastoma spheroids of different sizes. Br J Cancer 1992;66(6):1048–52.

[33] Almuhaideb A, Papathanasiou N, Bomanji J. ^{18}F-FDG PET/CT imaging in oncology. Ann Saudi Med 2011;31(1):3–13.

[34] Klug F, Prakash H, Huber PE, Seibel T, Bender N, Halama N, et al. Low-dose irradiation programs macrophage differentiation to an iNOS^{+}/M1 phenotype that orchestrates effective T cell immunotherapy. Cancer Cell 2013;24(5):589–602.

[35] Wang G, Wu Z, Wang Y, Li X, Zhang G, Hou J. Therapy to target renal cell carcinoma using ^{131}I-labeled B7-H3 monoclonal antibody. Oncotarget 2016;7(17):24888–98.

[36] Matsumura Y, Maeda H. A new concept for macromolecular therapeutics in cancer chemotherapy: mechanism of tumoritropic accumulation of proteins and the antitumor agent smancs. Cancer Res 1986;46(12 Pt 1):6387–92.

[37] Maeda H, Matsumura Y. EPR effect based drug design and clinical outlook for enhanced cancer chemotherapy. Adv Drug Deliv Rev 2011;63(3):129–30.

[38] Oh JR, Ahn BC. False-positive uptake on radioiodine whole-body scintigraphy: physiologic and pathologic variants unrelated to thyroid cancer. Am J Nucl Med Mol Imaging 2012;2(3):362–85.

[39] Liu Z, Xing M. Induction of sodium/iodide symporter (NIS) expression and radioiodine uptake in non-thyroid cancer cells. PLoS One 2012;7(2):e31729.

[40] Huang R, Zhao Z, Ma X, Li S, Gong R, Kuang A. Targeting of tumor radioiodine therapy by expression of the sodium iodide symporter under control of the survivin promoter. Cancer Gene Ther 2011;18(2):144–52.